Biomech Model Mechanobiol
DOI 10.1007/s10237-015-0731-8

ORIGINAL PAPER

Effect of ocular shape and vascular geometry on retinal hemodynamics: a computational model

Andrea Dziubek[1] · **Giovanna Guidoboni**[2,3,4] · **Alon Harris**[4] · **Anil N. Hirani**[5] · **Edmond Rusjan**[1] · **William Thistleton**[1]

Received: 31 July 2015 / Accepted: 23 September 2015

Abstract A computational model for retinal hemodynamics accounting for ocular curvature is presented. The model combines (i) a hierarchical Darcy model for the flow through small arterioles, capillaries and small venules in the retinal tissue, where blood vessels of different size are comprised in different hierarchical levels of a porous medium; and (ii) a one-dimensional network model for the blood flow through retinal arterioles and venules of larger size. The non-planar ocular shape is included by (i) defining the hierarchical Darcy flow model on a two-dimensional curved surface embedded in the three-dimensional space; and (ii) mapping the simplified one-dimensional network model onto the curved surface. The model is solved numerically using a finite element method in which spatial domain and hierarchical levels are discretized separately. For the finite element method, we use an exterior calculus-based implementation which permits an easier treatment of non-planar domains. Numerical solutions are verified against suitably constructed analytical solutions. Numerical experiments are performed to investigate how retinal hemodynamics is influenced by the ocular shape (sphere, oblate spheroid, prolate spheroid and barrel are compared) and vascular architecture (four vascular arcs and a branching vascular tree are compared). The model predictions show that changes in ocular shape induce non-uniform alterations of blood pressure and velocity in the retina. In particular, we found that (i) the temporal region is affected the least by changes in ocular shape, and (ii) the barrel shape departs the most from the hemispherical reference geometry in terms of associated pressure and velocity distributions in the retinal microvasculature. These results support the clinical hypothesis that alterations in ocular shape, such as those occurring in myopic eyes, might be associated with pathological alterations in retinal hemodynamics.

Keywords Mathematical modeling · Retinal hemodynamics · Hierarchical porous medium · Ocular curvature · Vascular network · Finite element exterior calculus

Mathematics Subject Classification 76S05 · 93A30 · 65N30 · 76M10

1 Introduction

The rapid advance of imaging technologies in ophthalmology is making available a continually increasing number of data regarding retinal morphology, hemodynamics and metabolism. An accurate and efficient interpretation of such data is the key to advancing the understanding of ocular diseases and their treatment. However, the clinical interpretation of retinal measurements is still very challenging. Many systemic and ocular factors combine to give rise to the observed data, and it is extremely difficult to single out their individual contributions during clinical and animal studies. Mathematical modeling is gaining more and more attention in the ophthalmic science, as it may help providing a quanti-

✉ Andrea Dziubek
dziubea@sunyit.edu

[1] Department of Mathematics and Sciences, State University of New York Polytechnic Institute, 100 Seymour Rd, Utica, NY 13502, USA

[2] Department of Mathematical Sciences, Indiana University Purdue University Indianapolis, Indianapolis, IN 46202, USA

[3] LABEX IRMIA, Université de Strasbourg, 67000 Strasbourg, France

[4] Eugene and Marilyn Glick Eye Institute, Indiana University School of Medicine, Indianapolis, IN 46202, USA

[5] Department of Mathematics, University of Illinois at Urbana Champaign, Urbana, IL 61801, USA

Published online: 07 October 2015

tative representation of the biophysical processes in the eye and their interwoven physiology. Here we use mathematical modeling to theoretically investigate how and to what extent different ocular shapes and vascular architectures will influence the model predictions for the retinal perfusion, i.e., hemodynamics in the microvasculature nourishing the retinal tissue.

The choice to study changes in ocular shape and vascular architecture is motivated by clinical observations. Alterations in ocular shape, as it occurs for example in myopia, are often associated with vascular abnormalities (Benavente-Perez et al. 2010; Mamikonian et al. 2013; Shimada et al. 2004) and with higher risks of severe ocular conditions, such as glaucoma (Galassi et al. 1998; Leske 2007), retinal detachment (Lin et al. 2013; Zafar et al. 2013) and maculopathy (Foster and Jiang 2014; Hsu et al. 2014). Architectural changes in the retinal vasculature are also often associated with ocular diseases, including glaucoma (Gugleta et al. 2013; Koh et al. 2010; Tham et al. 2013; Wu et al. 2013), diabetic retinopathy (Crosby-Nwaobi et al. 2012a, b; Habib et al. 2014) and myopia (Fledelius and Goldschmidt 2010; Lim et al. 2011).

Several theoretical approaches have been used to capture the details of the retinal vasculature, including network models, fractal models (based on Murray's law Murray 1926; Sherman 1981) and recently multi-fractal analysis Talu (2013). Interestingly, various modeling approaches have been proposed to model retinal blood flow (Arciero et al. 2013; Guidoboni et al. 2014; Sacco et al. 2011; Takahashi et al. 2009), and leverage information from fundus images to improve physically based models (Ganesan et al. 2010, 2011; Liu et al. 2000).

To the best of our knowledge, however, none of the currently available models describing retinal hemodynamics accounts for the curvature of the retinal surface, which is indeed the main novelty of our study from both the modeling and clinical viewpoints.

In this paper, we describe retinal perfusion via a multiscale approach. The blood flow in retinal arterioles and venules of larger size is described using a one-dimensional network model. The blood flow in the microcirculation, comprising small arterioles, capillaries and small venules, is described using a hierarchical Darcy flow model where blood vessels of different size correspond to hierarchical levels of different permeability (D'Angelo 2007; Vankan et al. 1997). We remark that indeed a poroelastic model would be more suitable for the description of retinal perfusion, since the retina is directly exposed to the action of the intraocular pressure which might alter vascular diameters and, consequently, retinal blood flow (Guidoboni et al. 2014). In this perspective, the Darcy model for the flow through a porous (rather than poroelastic) medium utilized here should be seen as an informative and necessary first step toward the development of more complex models.

In order to account for the non-planar ocular shape, the hierarchical Darcy flow model is defined on a two-dimensional curved surface embedded in the three-dimensional space, and the one-dimensional network model is mapped onto the curved surface. In particular, here we compare four different geometries of clinical interest: sphere, oblate spheroid, prolate spheroid and barrel (Moriyama et al. 2011).

We use finite elements to discretize the hierarchical variable and reduce the hierarchical Darcy flow equation to a coupled system of Darcy flow equations. We then use finite element exterior calculus to discretize the spatial variable and couple the system of hierarchical Darcy flow equations to the one-dimensional network model via delta functions. Finite element exterior calculus provides a convenient framework for problems on curved surfaces. In particular, we use the PyDEC (Bell and Hirani 2012) library for our numerical experiments.

The mathematical model is described in Sect. 2 and the numerical method adopted to solve the model is presented in Sect. 3. Numerical solutions are verified against suitably constructed analytical solutions in Sect. 4. The numerical results are presented and discussed in Sect. 5. Conclusions and future directions are outlined in Sect. 6.

2 Mathematical model

2.1 Hierarchical Darcy flow model

We describe the retinal tissue as a thin two-dimensional curved surface Ω embedded in a three-dimensional space. Therefore, $\mathbf{x} \in \Omega$ denotes a vector of spatial coordinates in $\mathbb{R}^3$.

The retinal microvasculature through the tissue is composed of a network of vessels of different diameter and is modeled as a hierarchical porous medium (Vankan et al. 1997). In this framework, blood vessels are considered as pores in the tissue, and a hierarchical variable θ, defined on the interval [0, 1], is introduced to represent the variations in diameters of the pores. Small arterioles and small venules, corresponding to the levels $\theta = 1$ and 0, respectively, are coupled with the one-dimensional network described in Sect. 2.3.

Blood flow takes place both in the spatial direction (through vessels of comparable radius) and the hierarchical direction (from arterioles to venules), so that model parameters and unknowns are functions of both spatial and hierarchical variables $\mathbf{x}$ and θ.

Here we consider the stationary problem, which consists of finding *spatial velocity* $\mathbf{v} = \mathbf{v}(\mathbf{x}, \theta)$, *hierarchical velocity*

$\omega = \omega(\mathbf{x}, \theta)$, and *pressure* $p = p(\mathbf{x}, \theta)$, by solving the following system:

$$\nabla \cdot (n_b \mathbf{v}) + \frac{\partial}{\partial \theta}(n_b \omega) = 0 \qquad \mathbf{x} \in \Omega, \theta \in (0, 1) \tag{1a}$$

$$n_b \mathbf{v} = -\mathbf{K} \nabla p \qquad \mathbf{x} \in \Omega, \theta \in (0, 1) \tag{1b}$$

$$n_b \omega = -\alpha \frac{\partial p}{\partial \theta} \qquad \mathbf{x} \in \Omega, \theta \in (0, 1) \tag{1c}$$

subject to the boundary conditions

$$(n_b \mathbf{v})(\mathbf{x}, \theta) \cdot \mathbf{n} = 0, \ \mathbf{x} \in \partial\Omega, \theta \in [0, 1] \tag{2a}$$

$$(n_b w)(\mathbf{x}, 0) = -G_v \Big(p(\mathbf{x}, 0) - p_v(\mathbf{x}) \Big), \quad \mathbf{x} \in \Omega \tag{2b}$$

$$(n_b w)(\mathbf{x}, 1) = -G_a \Big(p_a(\mathbf{x}) - p(\mathbf{x}, 1) \Big), \quad \mathbf{x} \in \Omega. \tag{2c}$$

Here n_b is the *tissue porosity or fluid volume fraction* (ratio between blood volume and total volume of blood and tissue in the reference volume of the porous medium), $-n_b\omega$ is the *tissue perfusion* (volume of blood flowing down in the hierarchy per unit tissue), $\mathbf{K}$ is the *spatial permeability tensor* and α is the *hierarchical permeability*. In general, porosity and permeability may depend both on $\mathbf{x}$ and θ. In the boundary conditions, $\mathbf{n}$ represents the vector normal to the outer boundary of the spatial tissue domain Ω, and G_v and G_a are the hydraulic conductances between lowest hierarchy and draining veins, and between the highest hierarchy and feeding arteries, respectively. Following D'Angelo (2007), we will express the hydraulic conductances as

$$G_v = \alpha_v \delta_v(\mathbf{x}) \quad \text{and} \quad G_a = \alpha_a \delta_a(\mathbf{x}) \tag{3}$$

where α_v and α_a are venous and arterial conductances and $\delta_v(\mathbf{x})$ and $\delta_a(\mathbf{x})$ are delta functions which differ from zero only where the feeding arteries and draining veins are located, respectively. The intravascular pressure in the feeding arteries and draining veins are denoted by $p_v(\mathbf{x})$ and $p_a(\mathbf{x})$, respectively, and α_v and α_a are scalar functions possibly varying with $\mathbf{x}$.

The well posedness of equations (1a)–(1c) with boundary conditions (2a)–(2c) with the delta function data of Eq. (3) is discussed in D'Angelo (2007). In this paper, we solve system 1 with the boundary conditions 2 on domains of different shape and for vascular tree of different geometries, as described in the following sections.

In order to facilitate the comparison between vascular trees of different geometry, it is useful to identify six regions of clinical interest in the retina, as schematized in Fig. 1. The major retinal vessels depart from the optic nerve head (ONH) and virtually divide the retina into four quadrants, referred to as the inferior (I), superior (S), nasal (N) and temporal (T) quadrants. The fovea, located in the temporal region, provides the sharpest vision and is avascular. The retinal image is taken from the DRIVE database (Staal et al. 2004).

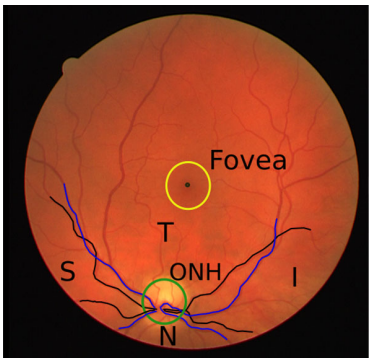

Fig. 1 Six regions of particular clinical interest in the retina: optic nerve head (ONH), inferior quadrant (I), superior quadrant (S), nasal quadrant (N), temporal quadrant (T) and fovea

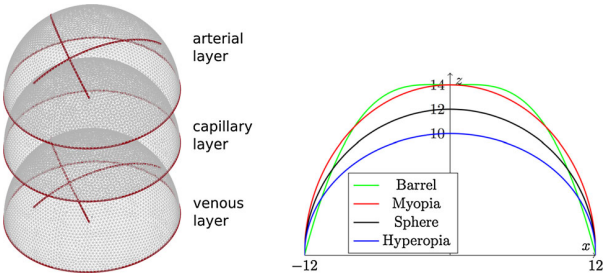

Fig. 2 (*Left*) Representation of three hierarchical levels, where four main arterioles are included as sources in the arterial level and four main venules are included as sinks in the venous level; (*right*) spherical, oblate ellipse, prolate ellipse and barrel shapes

2.2 Domain geometry

The reference geometry for the domain Ω is the hemispherical surface with radius $R = 12$ mm, representing a normal eye. In addition, we consider the following shapes (also depicted in Fig. 2):

1. *an oblate spheroid* with semi-axes $R = 12$ mm and $H = 10$ mm, representing an eye with shorter axial length (condition often associated with hyperopia);
2. *a prolate spheroid* with semi-axes $R = 12$ mm, $H = 14$ mm, representing an eye with longer axial length (condition often associated with myopia);
3. *a barrel-like surface* described by a polynomial of degree three $p_3(Z) = a_1 + a_2 Z + a_3 Z^2 + a_4 Z^3$ where $Z = \sqrt{x^2 + y^2}$ satisfying the conditions $p_3'(0) = 0$, $p_3(0) = H$, $p_3(\frac{R}{2}) = H - 1.3$ mm, $p_3(R) = 0$; representing an eye with longer axial length and flattened posterior sclera (another condition often associated with myopia).

2.3 Arterial and venous vascular tree geometry

Larger arterioles and venules are described using simplified one-dimensional models. Let us denote by Λ_a and Λ_v the collection of centerlines of the arterial and venous networks in the flat plane, respectively. The centerlines are then mapped onto the spherical surface as shown in Fig. 3. More precisely, every point (x_0, y_0) in Λ_a or Λ_v is mapped into a point on the sphere $(x_0, y_0, z_0 = \sqrt{x_0^2 + y_0^2})$. The resulting $\Gamma_a = \gamma_a(\Lambda_a)$ and $\Gamma_v = \gamma_v(\Lambda_v)$ lay on the curved surface, meaning that $\Gamma_a \subset \Omega \subset \mathbb{R}^3$ and $\Gamma_v \subset \Omega \subset \mathbb{R}^3$. We rotate the geometry of the remapped vascular networks by $\pi/4$ about the z axis followed by a rotation of $\pi/6$ about the x axis, so that the arcs originate from a point located at $x = 0$, $y = -R/2$ and $z = R\sqrt{3}/2$, representing the location of the optic nerve head (ONH). The same rotation is applied to the arterial and venous networks.

In this paper, we consider two vascular architectures embodying different levels of detail. The simplest architecture includes only four major feeding arteries and draining veins modeled as four arcs, see Fig. 2, along which a constant pressure is imposed. Here we consider $p_a = 33.75$ mmHg for arteries and $p_v = 16.4$ mmHg for veins. This simple vascular architecture is used to compare the numerical simulations obtained when varying the ocular shape, see Sect. 5.2.

A more realistic vascular model is obtained by applying the dichotomous tree approach proposed by Takahashi et al (2009) starting from the four major arcs mentioned above. Figure 3 (Left) shows the centerlines of a collection of binary trees joint at the root. The first four branches are 3.6 and 2.4 mm long. Branches of the following generations are scaled by 0.8, spatially arranged with angles of $\pi/6$, $\pi/8$, $\pi/10$, $\pi/12$ between parent/child and child/child branches. The angles are chosen to ensure that (i) the domain is well covered by the vascular tree, (ii) the foveal area is free of vessels and (iii) the ends of the binary trees are not too close to each other, see also Fig. 1.

At each branching point of the dichotomous tree, the relationship between the radius R_1 of the mother branch and the radii $R_{2,1}$ and $R_{2,2}$ of the two daughter branches is assumed to be:

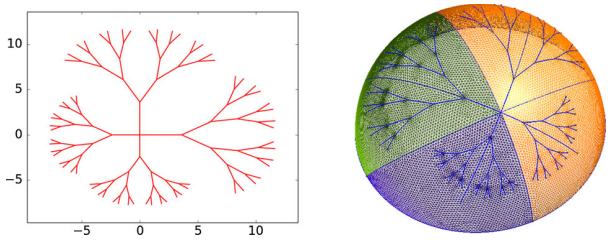

Fig. 3 (*Left*) Collection of binary trees joined at their roots on a flat domain; (*right*) binary trees mapped onto the spherical surface and meshed with Gmsh

Table 1 Pressures in mmHg at nodes of the vascular tree

Branching node	0	1	2	3	4
Arterial pressure	33.5	31.51	29.56	27.64	25.8
Venous pressure	16.4	18.39	20.34	22.26	24.1

$$R_1^m = R_{2,1}^m + R_{2,2}^m, \tag{4}$$

with $m = 2.85$ Murray (1926). The length L_j of each individual branch characterized by the radius R_j is calculated as

$$L_j(R_j) = \beta\, R_j^\eta, \tag{5}$$

where $\eta = 1.15$ and $\beta = 7.4$ (Takahashi et al. 2009).

In each vessel, we assume that: (i) the blood behaves as a Newtonian viscous fluid of viscosity μ; (ii) the flow is laminar, stationary and axially symmetric; and (iii) no-slip boundary conditions are imposed at the lateral vessel boundary. These assumptions allow us to write the blood pressure p inside each vessel as a function of the curvilinear coordinate s along the vessel centerline and to use Hagen-Poiseuille's law to calculate the pressure p as

$$p(s) = p_0 - \left(\frac{8\mu_j L_j}{\pi R_j^4}\right) Q_j\, s \quad \text{for } s \in [0, L_j] \tag{6}$$

where $s = 0$ and $s = L_j$ indicate the upstream and downstream ends of the vessel, p_0 is the upstream pressure and Q_j is the volumetric flow rate. We recall that mass conservation at each branch implies that $Q_g = 2Q_{g+1}$, where g is the generation of a branch.

Viscosity values per branch segment are linearly interpolated from viscosity values reported in Arciero et al. (2013), where $\mu = 2.28$ cPa in the larger arterioles and venules, and $\mu = 2.08$ cPa in the smaller arterioles and venules. Pressure values at the four main branches of the central retinal artery (CRA) and the central retinal vein (CRV) are assumed to be $p_{0a} = p_a = 33.75$ mmHg and $p_{0v} = p_a = 16.4$ mmHg, respectively, which is in agreement with Arciero et al. (2013). The average blood flow rate in the retina is assumed to be $\bar{Q}_{tot} = 36.11$ µl/min, as reported in the Table 2. For the blood flow rate after the first division into the four major branches, we assume $Q_0 = \bar{Q}_{tot}/4$.

Pressure values at the branching nodes of the binary tree are computed via (6) using the length of the branches in the flat plane and are summarized in Table 1. Note that 760.0 mmHg = 101.325 kPa.

The computational mesh for the domain Ω is generated with the Delaunay algorithm using Gmsh (Geuzaine and Remacle 2009), with additional functionality to ensure that

Table 2 Values of material and physical parameters in the hierarchical porous media model for the retinal circulation

Parameters	Arteries ($i = 2$)	Capillaries ($i = 1$)	Veins ($i = 0$)	Parameters	Value
Hierarchy (θ) [1]	1	1/2	0	Eye radius (R) [mm]	12
Number of pores (n_p) [1]	40	187890	40	Tissue thickness (h) [μm]	100
Pore diameter (D) [μm]	47.2	6.0	68.5	Total tissue volume (V_tot) [mm^3]	90.48
Pore length (L) [cm]	0.52	0.067	0.52	Arterial pressure (p_a) [mmHg]	33.75
Porosity (n_b) [1]	0.0040	0.0393	0.0085	Venous pressure (p_v) [mmHg]	16.4
Average velocity ($\bar{v}$) [cm/s]	0.86	0.011	0.41	Average blood flow rate ($\bar{Q}_\mathrm{tot}$) [μl/min]	36.11
Average pressure ($\bar{p}$) [mmHg]	28.75	21.23	17.56	Average tissue perfusion (ω_t) [1/s]	0.007
Conductance (α) [1/(s kPa)]	0.003	0.005	0.007	Arterial conductance (α_a) [1/(s kPa)]	0.006
Permeability (K) [mm^2/(s kPa)]	2	0.1	6	Venous conductance (α_v) [1/(s kPa)]	0.023

the centerlines Γ_a and Γ_v are along the edges of the triangulation while avoiding a distorted mesh.

3 Numerical method

3.1 Discretization of the hierarchical variable θ

To discretize the system 1 and 2 in the hierarchical variable, we follow the approach described in Vankan et al. (1997). We first write 1 in direct form with only pressure as the unknown:

$$-\nabla\cdot(\mathbf{K}\nabla p)-\frac{\partial}{\partial\theta}\left(\alpha\frac{\partial p}{\partial\theta}\right)=0(\mathbf{x},\theta)\in\Omega\times(0,1). \quad (7)$$

Let $\varphi = \varphi(\theta)$ be a smooth function defined on $[0, 1]$. To obtain the weak formulation, we multiply (7) by a test function $\varphi(\theta)$, integrate by parts over $[0, 1]$ and utilize the boundary conditions in θ to obtain:

$$\begin{aligned}&\int_0^1 -\nabla\cdot(\mathbf{K}(\mathbf{x},\theta)\nabla p(\mathbf{x},\theta))\,\varphi(\theta)+\alpha(\mathbf{x},\theta)\frac{\partial p(\mathbf{x},\theta)}{\partial\theta}\varphi'(\theta)\,\mathrm{d}\theta\\&\quad+\varphi(1)G_\mathrm{a}\,p(\mathbf{x},1)+\varphi(0)G_\mathrm{v}\,p(\mathbf{x},0)\\&\quad=\varphi(0)G_\mathrm{v}p_\mathrm{v}(\mathbf{x})+\varphi(1)G_\mathrm{a}p_\mathrm{a}(\mathbf{x}).\end{aligned} \quad (8)$$

Now, to obtain a semi-discrete model in the hierarchical variable θ, we introduce piecewise linear basis functions $\{\varphi_k\}$, with $k = 0, \ldots, n$ on $[0, 1]$ corresponding to nodes $\{\theta_k\}$. We write permeability, conductance and pressure as piecewise linear interpolations at the nodes of the discrete hierarchical variable, namely

$$\mathbf{K}(\mathbf{x},\theta)=\sum_{k=0}^{n}\mathbf{K}(\mathbf{x},\theta_k)\varphi_k(\theta), \quad (9a)$$

$$\alpha(\mathbf{x},\theta)=\sum_{k=0}^{n}\alpha(\mathbf{x},\theta_k)\varphi_k(\theta), \quad (9b)$$

$$p(\mathbf{x},\theta)=\sum_{k=0}^{n}p(\mathbf{x},\theta_k)\varphi_k(\theta). \quad (9c)$$

Substituting expressions (9a)–(9c) into (8) and considering a specific basis function $\varphi = \varphi_i$, we obtain the semi-discrete weak form

$$\sum_{j=0}^{n}-\nabla\cdot\left(\mathbf{K}_{ij}(\mathbf{x})\nabla p_j(\mathbf{x})\right)+\sum_{j=0}^{n}\alpha_{ij}(\mathbf{x})p_j(\mathbf{x})=f_i(\mathbf{x}) \quad (10)$$

where

$$\mathbf{K}_{ij}(\mathbf{x})=\sum_{k=0}^{n}\mathbf{K}(\mathbf{x},\theta_k)\int_0^1\varphi_k(\theta)\,\varphi_i(\theta)\,\varphi_j(\theta)\,\mathrm{d}\theta \quad (11a)$$

$$\begin{aligned}\alpha_{ij}(\mathbf{x})=&\sum_{k=0}^{n}\alpha(\mathbf{x},\theta_k)\int_0^1\varphi_k(\theta)\,\varphi_i'(\theta)\,\varphi_j'(\theta)\,\mathrm{d}\theta\\&+\delta_{i0}\delta_{j0}G_\mathrm{v}+\delta_{in}\delta_{jn}G_\mathrm{a}\end{aligned} \quad (11b)$$

$$f_i(\mathbf{x})=\delta_{i0}G_\mathrm{v}\,p_\mathrm{v}+\delta_{in}G_\mathrm{a}\,p_\mathrm{a} \quad (11c)$$

and where $p_j(\mathbf{x}) = p(\mathbf{x}, \theta_j)$ and δ_{ij} is the Kronecker delta. For each i and j, $\mathbf{K}_{ij}(\mathbf{x})$ is still a 2×2 matrix to potentially account for anisotropies in the tissue permeability. In this paper though, as in D'Angelo (2007), we neglect such anisotropy and we assume that permeability and conductivity depend only on θ. Then $\mathbf{K}(\theta) = K(\theta)\mathbf{I}$, which implies $\mathbf{K}_{ij} = K_{ij}\mathbf{I}$.

The hierarchical discretization leads to a tridiagonal system for the pressures $p_j(\mathbf{x})$ at each hierarchical node. In the case of three nodes, namely $j = 0, 1, 2$, we obtain

$$\begin{bmatrix}-K_{00}\Delta+\alpha_{00} & -K_{01}\Delta+\alpha_{01} & 0\\ -K_{10}\Delta+\alpha_{10} & -K_{11}\Delta+\alpha_{11} & -K_{12}\Delta+\alpha_{12}\\ 0 & -K_{21}\Delta+\alpha_{21} & -K_{22}\Delta+\alpha_{22}\end{bmatrix}\begin{bmatrix}p_0\\p_1\\p_2\end{bmatrix}=\begin{bmatrix}f_0\\f_1\\f_2\end{bmatrix} \quad (12)$$

where the scalar K_{ij} is the ij entry of the matrix

$$\frac{1}{24}\begin{bmatrix} 3K_0+K_1 & K_0+K_1 & 0 \\ K_0+K_1 & K_0+6K_1+K_2 & K_1+K_2 \\ 0 & K_1+K_2 & K_1+3K_2 \end{bmatrix},$$

the scalar α_{ij} is the ij entry of the matrix

$$\begin{bmatrix} \alpha_0+\alpha_1+G_\mathrm{v} & -(\alpha_0+\alpha_1) & 0 \\ -(\alpha_0+\alpha_1) & \alpha_0+2\alpha_1+\alpha_2 & -(\alpha_1+\alpha_2) \\ 0 & -(\alpha_1+\alpha_2) & \alpha_1+\alpha_2+G_\mathrm{a} \end{bmatrix},$$

and the scalar f_i is the i component of the vector

$$\left[G_\mathrm{v} p_\mathrm{v}, 0, G_\mathrm{a} p_\mathrm{a}\right]^T.$$

Here $\alpha_0, \alpha_1, \alpha_2$ and K_0, K_1, K_2 are the conductivities and permeabilities at the three hierarchical levels and are given in Eq. (24) and (26).

The homogeneous Neumann boundary conditions (2a) complete the system. Note that the Robin pressure conditions (2b) and (2c) contribute to the two terms α_{ij} and f_i.

3.2 Spatial discretization using exterior calculus

Equation (12) can be written as a system for each θ level i (using Einstein notation)

$$-K_{ij}\,\Delta\, p_j + \alpha_{ij}\, p_j = f_i \tag{13}$$

and the systems obtained for each i have to be solved simultaneously as indicated in Eq. (12).

To carry out the discretization of the spatial operator Δ in (13), there are several alternatives even within the framework of finite element methods. The domain Ω is a curved surface embedded in $\mathbb{R}^3$ and so the Laplacian operator Δ in Eq. (13) is the Laplace–Beltrami operator. One approach toward discretizing the Laplace–Beltrami operator is via surface finite element methods (Demlow 2009; Demlow and Dziuk 2007; Dziuk 1988). Another systematic framework is the use of exterior calculus discretization, and this is the one we follow in this paper. Exterior calculus is a generalization of calculus to manifolds and allows the definition of differential operators in a coordinate invariant manner, which can then be discretized by intrinsic computation of quantities in the triangles approximating the surface.

For computational purposes, exterior calculus has been discretized as finite element exterior calculus (Arnold et al. 2010) and discrete exterior calculus (Desbrun 2005; Hirani 2003). These discretizations are useful either when a mixed method (involving both velocities and pressures) is to be implemented or when the domain is not flat, as is the case in this paper. They have been implemented in the software package PyDEC (Bell and Hirani 2012), which we used for our computations.

We discretize the first term on the left-hand side of Eq. (13) using finite element exterior calculus. Since Eq. (13) involves a pressure-only formulation, the resulting matrix is identical to the one obtained by a standard finite element formulation. The matrix corresponding to $-K_{ij}\Delta p_j$ in the left-hand side of Eq. (13) is

$$K_{ij}\,\mathbf{d}_0^T *_1 \mathbf{d}_0\, p_j. \tag{14}$$

Here $\mathbf{d}_0^T *_1 \mathbf{d}_0$ is the usual stiffness matrix of standard piecewise linear finite element method. The matrix $\mathbf{d}_0$ has N_1 rows and N_0 columns, where N_1 is the number of edges in the triangulation approximation of Ω and N_0 is the number of vertices in the triangulation. Each column corresponds to a vertex and the entries are $+1$, -1 or 0, depending on if that vertex belongs to the head of an edge, its tail, or not at all. The matrix $*_1$ is of size $N_1 \times N_1$ and is obtained by computing inner products of Whitney forms, also known as edge elements. See Bell and Hirani (2012) for details.

We now describe the discretization of the $\delta_{i0}\delta_{j0}G_\mathrm{v}$ and $\delta_{in}\delta_{jn}G_\mathrm{a}$ terms in Eq. (11b) and the discretization of the right-hand side f_i. The terms $\delta_{i0}G_\mathrm{v}p_\mathrm{v}$ and $\delta_{in}G_\mathrm{a}p_\mathrm{a}$ on the right-hand side are the prescribed venous and arterial pressures at the vertices corresponding to the edges of the triangulation of veins and arteries. In the discretization, we consider the values at vertices to be piecewise constant, with each such constant value extending from the vertex to the midpoint of all edges containing that vertex. The terms $\delta_{i0}\delta_{j0}G_\mathrm{v}$ and $\delta_{in}\delta_{jn}G_\mathrm{a}$ are treated the same way. This is achieved by defining the matrix $\mathbb{E}$ to be a diagonal matrix of size $N_0 \times N_0$. The nonzero diagonal entry corresponding to a vertex is 0.5 times the sum of lengths of edges containing that vertex. Then the terms $\alpha_{ij}\,p_j$ on the left-hand side of (13) are discretized as

$$*_0\alpha_{ij}\,p_j + \mathbb{E}\Big(\delta_{i0}\delta_{j0}\alpha_\mathrm{v} + \delta_{in}\delta_{jn}\alpha_\mathrm{a}\Big)\,p_j \tag{15}$$

and f_i on right-hand side of (13) is discretized as

$$\mathbb{E}\Big(\delta_{i0}\alpha_\mathrm{v}\, p_\mathrm{v} + \delta_{in}\alpha_\mathrm{a}\, p_\mathrm{a}\Big) \tag{16}$$

where p_a and p_v contains the values of prescribed pressures sampled at the vertices. Here $*_0$ is the usual mass matrix of standard piecewise linear finite elements. Thus the complete discretization of (13) is

$$\begin{aligned} &\sum_{j=0}^{n} K_{ij}\mathbf{d}_0^T *_1 \mathbf{d}_0 p_j \\ &\quad + *_0\alpha_{ij}\, p_j + \mathbb{E}(\delta_{i0}\delta_{0j}\alpha_\mathrm{v} + \delta_{in}\delta_{nj}\alpha_\mathrm{a})\,p_j \\ &= \mathbb{E}\Big(\delta_{i0}\alpha_\mathrm{v}\, p_\mathrm{v} + \delta_{in}\alpha_\mathrm{a}\, p_\mathrm{a}\Big). \end{aligned} \tag{17}$$

One of the authors recently showed that a formulation based on exterior calculus is very effective in simulating Darcy flow on curved surfaces (Hirani and Nakshatrala 2015). However, the computational approach in the present article differs from that discussed in Hirani and Nakshatrala (2015) since here we consider the following: (i) an extension of the Darcy equations to the flow through a hierarchical porous medium, thereby requiring suitable discretization of the corresponding hierarchical variable θ; (ii) source terms distributed along the centerlines of the vascular trees, thereby requiring suitable discretization of the corresponding delta functions. In addition, we remark that the method in Hirani and Nakshatrala (2015) relies on a mixed formulation of the problem, whereas here we solve for the pressure as the sole primal variable.

3.3 Pullback of the velocity field to the sphere

To compare the velocity fields defined on different domain geometries, we pull back all velocity fields to the sphere. The velocities $\mathbf{u} = \left[u_1, u_2, u_3\right]^T$ from the oblate and the prolate ellipsoidal surface are pulled back to the spherical surface by a simple scaling $\mathbf{v} = \left[u_1, u_2, u_3 \frac{H}{R}\right]^T$. To pull the velocities from the barrel-shaped surface back to the sphere, we extend the map from the sphere to the barrel-shaped surface $\phi\colon S^2 \to B^2$ to a map in three dimensions $\Phi\colon \mathbf{P}(\mathbf{Q}) \to \mathbf{p}(\mathbf{q})$, where $\mathbf{Q}, \mathbf{q} \in \mathbb{R}^2$ and $\mathbf{P}, \mathbf{p} \in \mathbb{R}^3$. Tangent vectors are pushed forward by the differential of the map $\mathbf{v} = \Phi_* (\mathbf{V}) = D\Phi\,(\mathbf{V}) = \mathbf{F}\mathbf{V}$. The map and its differential are given by

$$\Phi\colon \begin{bmatrix} X \\ Y \\ Z \end{bmatrix} \to \begin{bmatrix} x = X \\ y = Y \\ z = p_3(Z) \end{bmatrix} \qquad D\Phi = \begin{bmatrix} 1 & & \\ & 1 & \\ & & \frac{\partial z}{\partial Z} \end{bmatrix}$$

where $z = p_3(Z)$ is the polynomial of degree three describing the barrel shape, see Fig. 4. Note that the map is not invertible for some values $\frac{\partial z}{\partial Z} = 0$, so we cannot compute the inverse of $\mathbf{F}$ to pull back the barrel velocity to the sphere but instead need to go 'backwards':

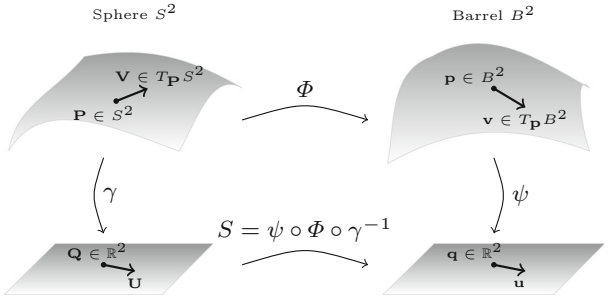

Fig. 4 Map from sphere to barrel-shaped surface

$$\mathbf{V} = \Phi^* (\mathbf{v}) = D\gamma^{-1} \circ DS^{-1} \circ D\psi\,(\mathbf{v}) = \begin{bmatrix} v_1 \\ v_2 \\ \frac{-v_1 x - v_2 y}{\sqrt{R^2 - x^2 - y^2}} \end{bmatrix}.$$

4 Verification of the numerical strategy

We construct here two ad hoc analytical solutions to the coupled problem 1 and 2 in order to test our numerical strategy. In particular, we want to verify the correctness of our numerical implementation with respect to:

1. the boundary conditions in 2 along the vessels Γ_{v} and Γ_{a} involving delta functions $\delta_{\Gamma_{\mathrm{v}}}$ and $\delta_{\Gamma_{\mathrm{a}}}$;
2. combining the hierarchical and spatial discretization using finite elements and discrete exterior calculus matrices.

4.1 Testcase to verify the discretization of the boundary conditions along the vessels Γ_{v} and Γ_{a} involving delta functions $\delta_{\Gamma_{\mathrm{v}}}$ and $\delta_{\Gamma_{\mathrm{a}}}$

The boundary conditions involving delta functions are those pertaining to the θ-direction, see (2b) and (2c). When performing the semi-discretization of the problem, these boundary conditions become part of the right-hand side for a differential problem in space, as shown in (13). Thus, in order to test the accuracy of the numerical method, it is enough to consider the following Poisson problem with a Dirac source term:

$$\begin{aligned} \Delta p &= \delta_{\Gamma_{\mathrm{c}}} \quad \text{in } \Omega_{\mathrm{c}} \\ p &= 0 \quad\;\; \text{on } \partial\Omega_{\mathrm{c}} \end{aligned} \tag{18}$$

where, for simplicity, we assume that Ω_{c} is the planar circle of radius R_{c} centered at the origin, and that Γ_{c} is its horizontal diameter. Thus we can write

$$\Omega_{\mathrm{c}} = \{\mathbf{x} = (x_1, x_2)\,|\,x_1^2 + x_2^2 < R_{\mathrm{c}}^2\},$$
$$\Gamma_{\mathrm{c}} = \{\mathbf{x} \in \Omega_{\mathrm{c}}\,|\,x_2 = 0\}.$$

An analytical solution to problem (18) can be constructed using standard techniques in partial differential equations (Evans 1998). The solution p is written as the sum of two parts, namely $p = v + u$, where v accounts for the Dirac source in Ω_{c} and u accounts for the boundary conditions on $\partial\Omega_{\mathrm{c}}$. More precisely, v is the convolution of the fundamental solution $k(\mathbf{x}) = \frac{1}{2\pi}\log|\mathbf{x}|$ with the source $f(\mathbf{x}) = \delta_{\Gamma_{\mathrm{c}}}$, namely

$$\begin{aligned} v(\mathbf{x}) &= \int_{\Omega_{\mathrm{c}}} k(\mathbf{x} - \mathbf{y})\, f(\mathbf{y})\, \mathrm{d}\mathbf{y} \\ &= \int_{\Omega_{\mathrm{c}}} \frac{1}{2\pi} \log|\mathbf{x} - \mathbf{y}| \delta_{\Gamma_{\mathrm{c}}}(\mathbf{y})\, \mathrm{d}\mathbf{y}, \end{aligned}$$

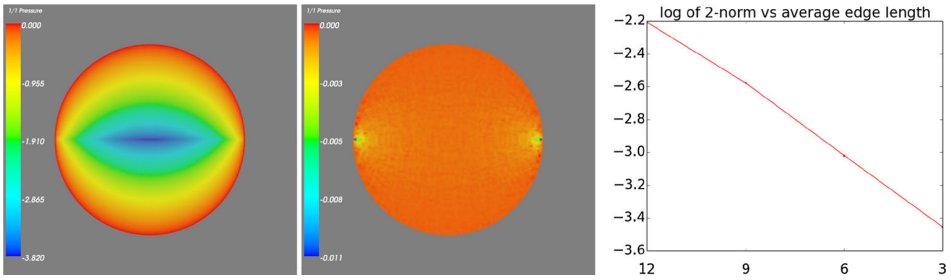

Fig. 5 (*Left*) Colorplot of the analytical solution (19) for the pressure satisfying problem (18); (*center*) Colorplot of the difference between analytical and numerical solution for the pressure satisfying problem (18); (*right*) logarithm of the Frobenius norm of the difference between analytical and numerical solutions for the pressure satisfying problem (18)

and u satisfies the Laplace's equation $\Delta u = 0$ in Ω_c, with $u = -v$ on $\partial\Omega_c$, which can be solved with the Poisson formula

$$u(\mathbf{x}) = \frac{R_c^2 - |\mathbf{x}|^2}{2\pi} \int_{|\boldsymbol{\xi}|=R_c} \frac{g(\boldsymbol{\xi})}{|\boldsymbol{\xi} - \mathbf{x}|^2} \, \mathrm{d}(\partial\Omega_a)$$

using polar coordinates $\boldsymbol{\xi} = \langle R_c \cos\psi, R_c \sin\psi \rangle$. In summary, the analytical solution $p = v + u$ is given by

$$p(\mathbf{x}) = \frac{1}{4\pi} \int_{\Gamma_c} \log\left((x_1 - y_1)^2 + x_2^2\right) + \frac{R_c^2 - |\mathbf{x}|^2}{2\pi} \int_{\partial\Omega_c} \frac{g(\boldsymbol{\xi})}{|\boldsymbol{\xi} - \mathbf{x}|^2} d\boldsymbol{\xi}. \tag{19}$$

To test our numerical solver, we compute a numerical solution of (18) by solving (17) on a planar circle with $R_c = 12$ mm, $K = 1$ mm^2/(s kPa), $\alpha_{ij} = 0$ (s kPa)$^{-1}$, and with homogeneous boundary conditions. A colorplot of the analytical solution (19) is reported in Fig. 5 (Left), whereas the difference between analytical and numerical solutions (obtained for an average edge length of 3 mm) is portrayed in Fig. 5 (Right). We notice that the largest errors are located around the points $(-R, 0)$ and $(R, 0)$. This is due to the fact that the analytical solution embodies the delta source term on the whole interval $[-R, R]$, whereas the numerical solution accounts for the delta source term only on the interval $[-(R - \mathrm{cl}), R - \mathrm{cl}]$, where cl is the average edge length (i.e., excluding the two boundary points where homogeneous dirichlet boundary conditions are imposed). Figure 5 (Center) shows that the logarithm of the Frobenius norm of the difference between numerical and analytical solutions is decreasing with the average mesh size. Here we have considered average edge length of 12, 9, 6 and 3 mm. The slope is roughly -1, which is consistent with a first-order method.

4.2 Testcase to verify the hierarchical and spatial discretization using finite elements and discrete exterior calculus matrices

Let us consider again $\Omega = \Omega_c$, where Ω_c is the planar circle of radius R_c. Thus, in polar coordinates we can define the cylinder $\mathcal{Q}_c = \Omega_c \times (0, 1)$ as

$$\mathcal{Q}_c = \{(r, \psi, \theta) \,|\, 0 \le r < R_c,\ 0 \le \psi < 2\pi,\ 0 < \theta < 1\}.$$

Let us denote by Σ_l the lateral surface of the cylinder, and by Σ_b and Σ_t the bottom and top circular surfaces, respectively. Let us define the lines $\Gamma_v \subset \Sigma_b$ and $\Gamma_a \subset \Sigma_t$ as

$$\Gamma_v = \{(r, \psi, \theta) \,|\, 0 \le r \le R_c, \quad \psi = \pi/2 \text{or} \psi = 3\pi/2, \theta = 0\},$$
$$\Gamma_a = \{(r, \psi, \theta) \,|\, 0 \le r \le R_c, \quad \psi = 0 \text{ or } \psi = \pi, \theta = 1\}.$$

Then we consider the following simplified problem

$$-K(\theta)\left(\frac{1}{r}\frac{\partial}{\partial r}\left(r\frac{\partial p}{\partial r}\right) + \frac{1}{r^2}\frac{\partial^2 p}{\partial \psi}\right) - \alpha(\theta)\frac{\partial^2 p}{\partial \theta^2} = f \tag{20}$$

defined in $\mathcal{Q}_c$, where f is a given scalar function. We construct an analytical solution to (20) subject to the following boundary conditions:

$$\begin{aligned} &\frac{\partial p}{\partial r} = 0 \quad \text{on} \quad \Sigma_l,\ \Sigma_b \setminus \Gamma_v \text{ and } \Sigma_t \setminus \Gamma_a, \\ &p = p_v \quad \text{on} \quad \Gamma_v, \\ &p = p_a \quad \text{on} \quad \Gamma_a. \end{aligned} \tag{21}$$

If the function f in (20) is given by

$$f(r, \psi, \theta) = K(\theta)\frac{b(\theta) - a(\theta)}{r^2}\sin(2\psi) - \alpha(\theta)\left(\frac{\partial^2 a}{\partial \theta^2}\cos^2\psi + \frac{\partial^2 b}{\partial \theta^2}\sin^2\psi\right) \tag{22}$$

where $\alpha(\theta) = \alpha_a\theta + (1 - \theta)\alpha_v$, $K(\theta) = K_a\theta + (1 - \theta)K_v$, $a(\theta) = \bar{p} + 3(p_a - \bar{p})\theta^2 - 2(p_a - \bar{p})\theta^3$, $\bar{p} = (p_a + p_v)/2$, and $b(\theta) = p_v + 3(\bar{p} - p_v)\theta^2 - 2(\bar{p} - p_v)\theta^3$, the problem admits the exact solution

$$p(\psi, \theta) = a(\theta)\cos^2\psi + b(\theta)\sin^2\psi. \tag{23}$$

We set $p_a = 20$ mmHg, $p_v = 10$ mmHg, $R_c = 12$ mm, $K_a = K_v = 1$ mm^2/(s kPa), and $\alpha_a = \alpha_v = 1$ (s kPa)$^{-1}$.

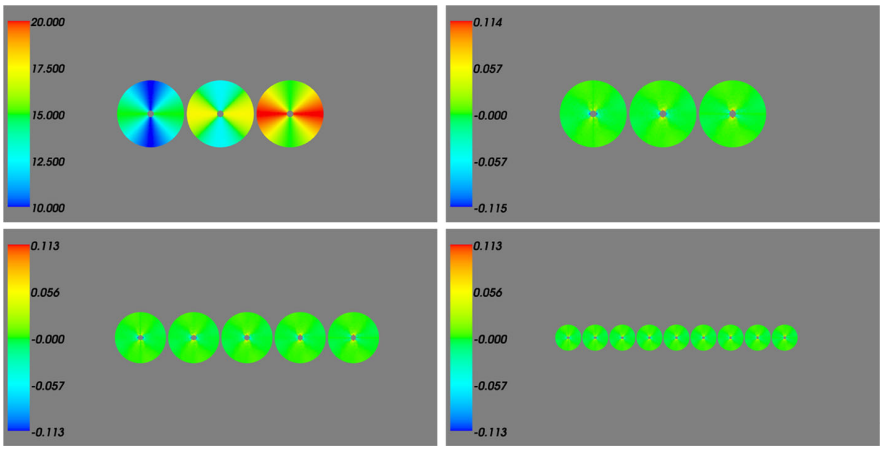

Fig. 6 (*Top left*) *Colorplot* of the numerical solution computed for problem (20) with the boundary conditions (21) and right-hand side(22), in the case of 3 θ-levels. Difference between numerical and analytical solutions computed for problem (20) with the boundary conditions (21) and right-hand side (22), in the case of 3 θ-levels (*top right*), 5 θ-levels (*bottom left*) and 9 θ-levels (*bottom right*)

To obtain a numerical solution, we solve (17) with the right-hand side vector (22). We assume $K_{ij} = 1$ mm^2/(s kPa) and $\alpha_{ij} = \alpha_{\mathrm{v}} = \alpha_{\mathrm{a}} = 1$ (s kPa)$^{-1}$. A colorplot of the numerical solution is reported in Fig. 6 (Top Left) in the case of 3 θ-levels. The remaining panels in Fig. 6 show that the difference between numerical and analytical solutions is less than 2 % when 3, 5 and 9 θ-levels are considered. Convergence was decided to be obtained when further mesh refinements do no change the solution. Average mesh element length is 0.5 mm. For visualization of the results, we used Mayavi Ramachandran et al. (2011).

5 Results of the numerical experiments

In this Section, we utilize our computational model to theoretically investigate some interesting features of retinal hemodynamics. We consider three hierarchical levels corresponding to arterioles ($\theta = 1$), capillaries ($\theta = 1/2$) and venules ($\theta = 0$), see also Fig. 2. Values for material and physical properties pertaining to each level are provided in Sect. 5.1. Numerical experiments investigating how retinal hemodynamics is influenced by the domain geometry and vascular architecture are presented in Sects. 5.2 and 5.3.

5.1 Porosity, conductance and permeability

We utilize the theory of capillary models for porous media (Causin et al. 2014; Huyghe et al. 1992), and we write the porosity at each hierarchical level as

$$n_{\mathrm{b}}(\theta) = \frac{n_{\mathrm{p}}(\theta)\pi D(\theta)^2 L(\theta)}{4V_{\mathrm{tot}}}$$

where n_p is the number of pores in the volume, D is the pore diameter, L is the length of pores and $V_{\mathrm{tot}} = 4\pi R^2 h/2$ is the total tissue volume, with R denoting the eye radius and h denoting the tissue thickness. We have assumed here that n_p and D are constant in space and depend only on the hierarchical level θ. Using the values from Arciero et al. (2013) reported also in Table 2, we obtain the following estimates for $n_{\mathrm{b}}(\theta_i) = n_{\mathrm{b}i}$:

$$n_{\mathrm{b}2} = 0.0040, \quad n_{\mathrm{b}1} = 0.0393, \quad n_{\mathrm{b}0} = 0.0085.$$

Conductances between adjacent hierarchical levels can be estimated knowing average pressure drops $\Delta\bar{p}_i$ and mean tissue perfusion ω_{t} between levels as

$$\alpha_i \simeq \omega_{\mathrm{t}} \frac{\Delta\theta_i}{\Delta\bar{p}_i}$$

with $\omega_{\mathrm{t}} = \bar{Q}_{\mathrm{tot}}/V_{\mathrm{tot}}$ defined as the average blood volume flow rate ($\bar{Q}_{\mathrm{tot}}$) per unit tissue volume (V_{tot}). Using again the values reported in Table 2, we obtain $\omega_{\mathrm{t}} = 0.007$ s^{-1} and, as a consequence, observing that $\Delta\theta_i = 1/2$, the following estimates for α_i in (s kPa)$^{-1}$ can be deduced:

$$\alpha_2 = \frac{\omega_{\mathrm{t}}}{2(\bar{p}_2 - \bar{p}_1)} = 0.003, \quad \alpha_1 = \frac{\omega_{\mathrm{t}}}{\bar{p}_2 - \bar{p}_0} = 0.005,$$
$$\alpha_0 = \frac{\omega_{\mathrm{t}}}{2(\bar{p}_1 - \bar{p}_0)} = 0.007. \tag{24}$$

Venous and arterial conductances α_{v} and α_{a} are estimated analogously, to obtain

$$\alpha_{\mathrm{a}} = \frac{\omega_{\mathrm{t}}}{2(\bar{p}_{\mathrm{a}} - \bar{p}_2)} = 0.006, \quad \alpha_{\mathrm{v}} = \frac{\omega_{\mathrm{t}}}{2(\bar{p}_0 - \bar{p}_{\mathrm{v}})} = 0.023, \tag{25}$$

again in (s kPa)$^{-1}$.

The permeability values at each hierarchical level $K(\theta_i) = K_i$ are chosen as to obtain physiologically reasonable velocity distribution at the capillary levels of the hierarchy when the spherical geometry is considered, see Fig. 2. Here we used

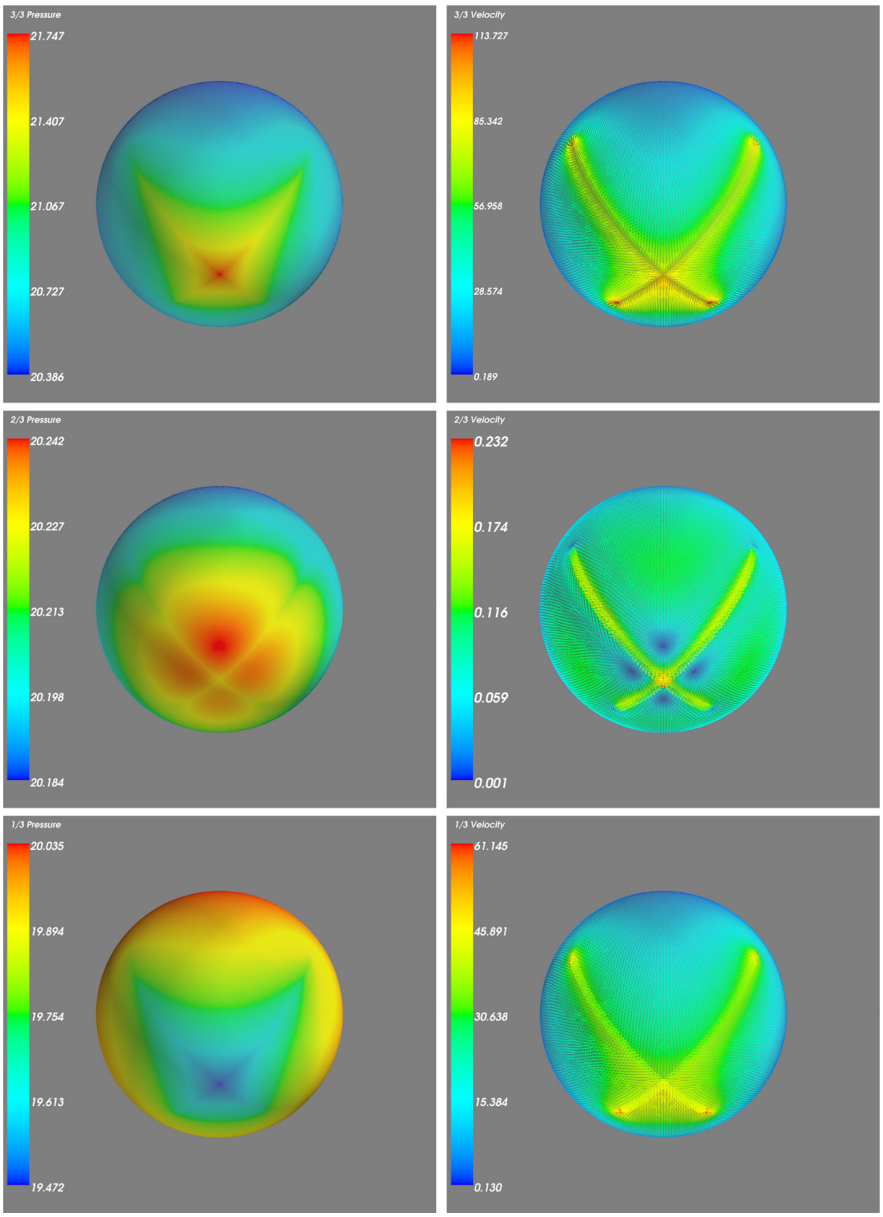

Fig. 7 Pressure fields in mmHg (*left*) and velocity fields in mm/s (*right*) for arterial (*top*), capillary (*middle*) and venous (*bottom*) level: hemispherical surface with major feeding arteries as four source terms in the arterial level with $p_a = 33.75$ mmHg and the major draining veins as four source terms in the venous level with $p_v = 16.4$ mmHg

$$K_2 = 2, \quad K_1 = 0.1, \quad K_0 = 6, \tag{26}$$

measured in $\text{mm}^2/(\text{s kPa})$.

5.2 Influence of domain geometry

We report in this Section solutions to 1 and 2 obtained with the parameters described in Sect. 5.1 in the case of the four different domain geometries described in Sect. 2.2. Here the arterial and venous vascular networks are modeled as four major arcs, as described in Sect. 2.3 and depicted in Fig. 2.

Simulated pressure fields and velocity fields in the reference case of hemispherical geometry are reported in Fig. 7. For all the three hierarchical levels corresponding to arterioles, capillaries and venules, pressures and velocities are within physiological ranges and, in particular, are of the same order of magnitude as those reported in Arciero et al. (2013).

Differences in pressure fields and velocity fields between the non-spherical geometries and the hemispherical reference model are reported in Fig. 8. We focus here on the capillary level, since it is the most important level for tissue perfusion and metabolism. We remark that the velocity fields are obtained by subtracting velocity field pullbacks to the sphere, as described in Sect. 3.3. Even though the distributions of velocity and pressure for the four cases look similar, interesting similarities and differences can be noticed when they are compared to the sphere, see Fig. 8.

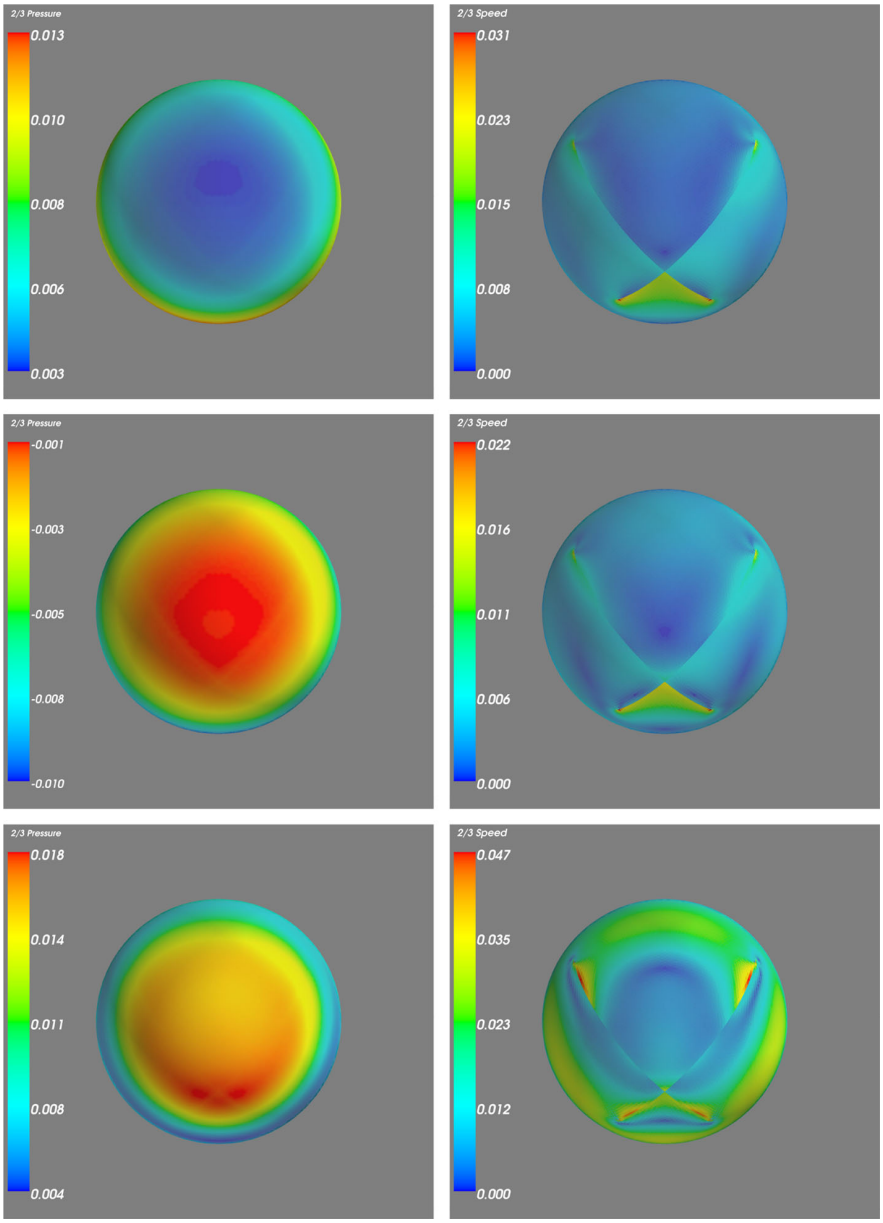

Fig. 8 Pressure differences in mmHg (*left*) and differences in the magnitude of velocities in mm/s (*right*) at the capillary level between (*top to bottom*) oblate spheroid and sphere, prolate spheroid and sphere, barrel and sphere

Overall, the blood velocity in the temporal region is less impacted by changes in domain geometry, i.e., ocular shape, since negligible differences are predicted in the velocity fields between non-spherical and spherical geometry for all cases, see Fig. 8. The largest difference from the velocity field calculated for the sphere is reported for the barrel geometry, see Fig. 8 (bottom), where nasal, inferior and superior regions exhibit differences up to 0.045 mm/s, corresponding to a 30 % increase with respect to the sphere.

Pressure differences are largest near the ONH, where the maximal pressure difference reaches 0.015 mmHg for barrel geometry. The precision of the computed pressure values in the capillary level is 1e−6 mmHg, and therefore, the predicted differences are significant from the numerical viewpoint.

5.3 Influence of vascular architecture

The four arcs model for the arterial and venous network utilized in the previous Section is indeed an extreme simplification of real vascular architectures. It is reasonable to hypothesize that different modeling choices for the vascular architecture would influence retinal perfusion. In this Section, we compute pressure and velocity fields obtained in the case of reference hemispherical geometry with the arterial (resp. venous) network modeled as

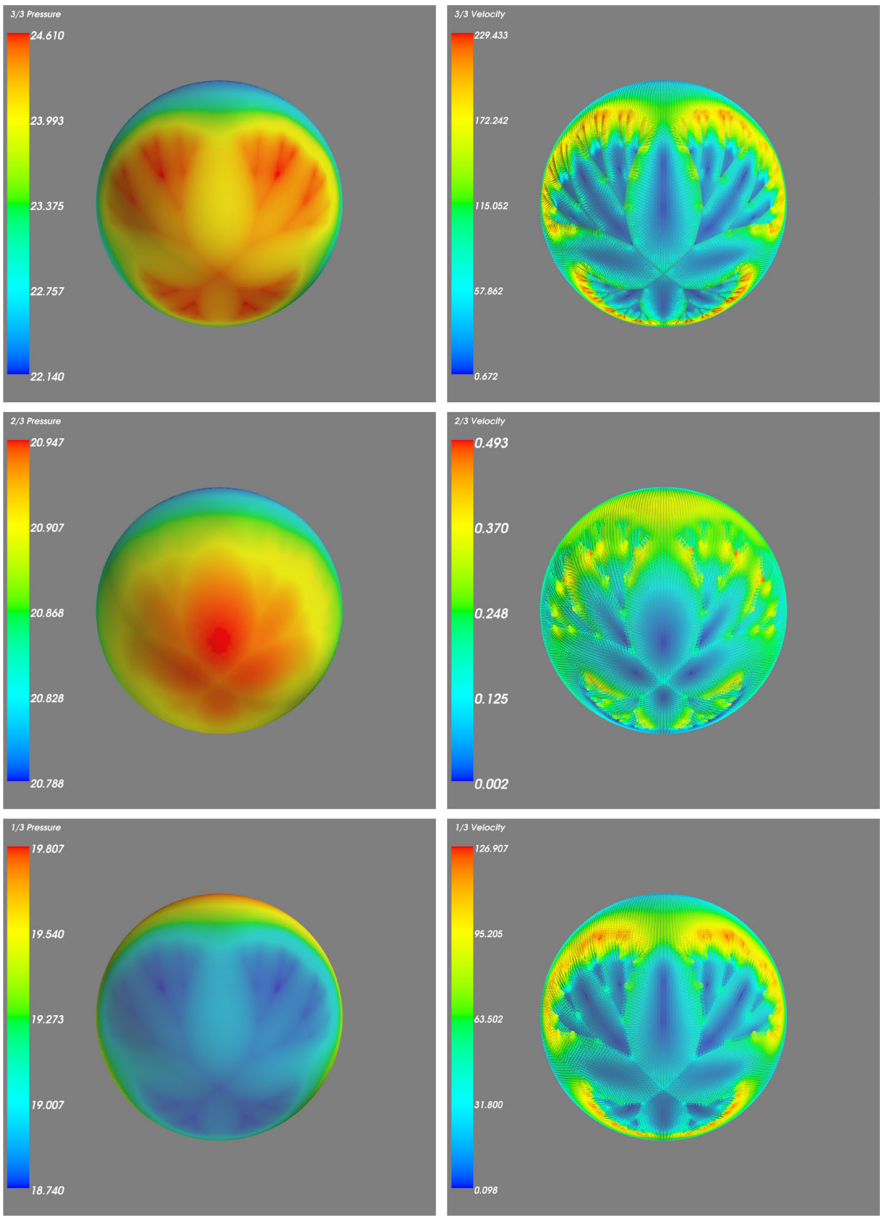

Fig. 9 Pressure fields in mmHg (*left*) and velocity fields in mm/s (*right*) for arterial, capillary and venous level. Binary tree model with same pressure on all arc segments ($p_a = 33.75$ mmHg for arterioles and $p_v = 16.4$ mmHg for venules)

binary trees stemming from (resp. merging into) the four major branches of the central retinal artery (resp. vein) as depicted in Fig. 3. For the above-described domain geometry and vascular architecture, we consider two different modeling choices for the pressure distribution along the network:

1. the pressure is constant in arterioles and venules, $p_a = 33.75$ mmHg and $p_v = 16.4$ mmHg, respectively. Results are reported in Fig. 9;
2. the pressure decreases linearly along the network according to the Poiseuille law (6), see also Table 1. Results are reported in Fig. 10.

Figures 9 and 10 show similar pressure and velocity ranges when compared with the reference model with the four arcs, see Fig. 7. Velocities are higher when the pressure is assumed constant along the vascular network, see Fig. 9, when compared to the case with linear pressure distribution, see Fig. 10.

It is very encouraging to find that reasonable pressure and velocity fields are obtained not only in the simple case of the four arcs, but also when a more complex vascular network is considered. The next step would be considering image-based vascular network to test the viability of patient-specific simulations. Photographically acquired fundus images are widely used in the clinical setting to help determine the health of the retina, and to track retinal changes over time. Support

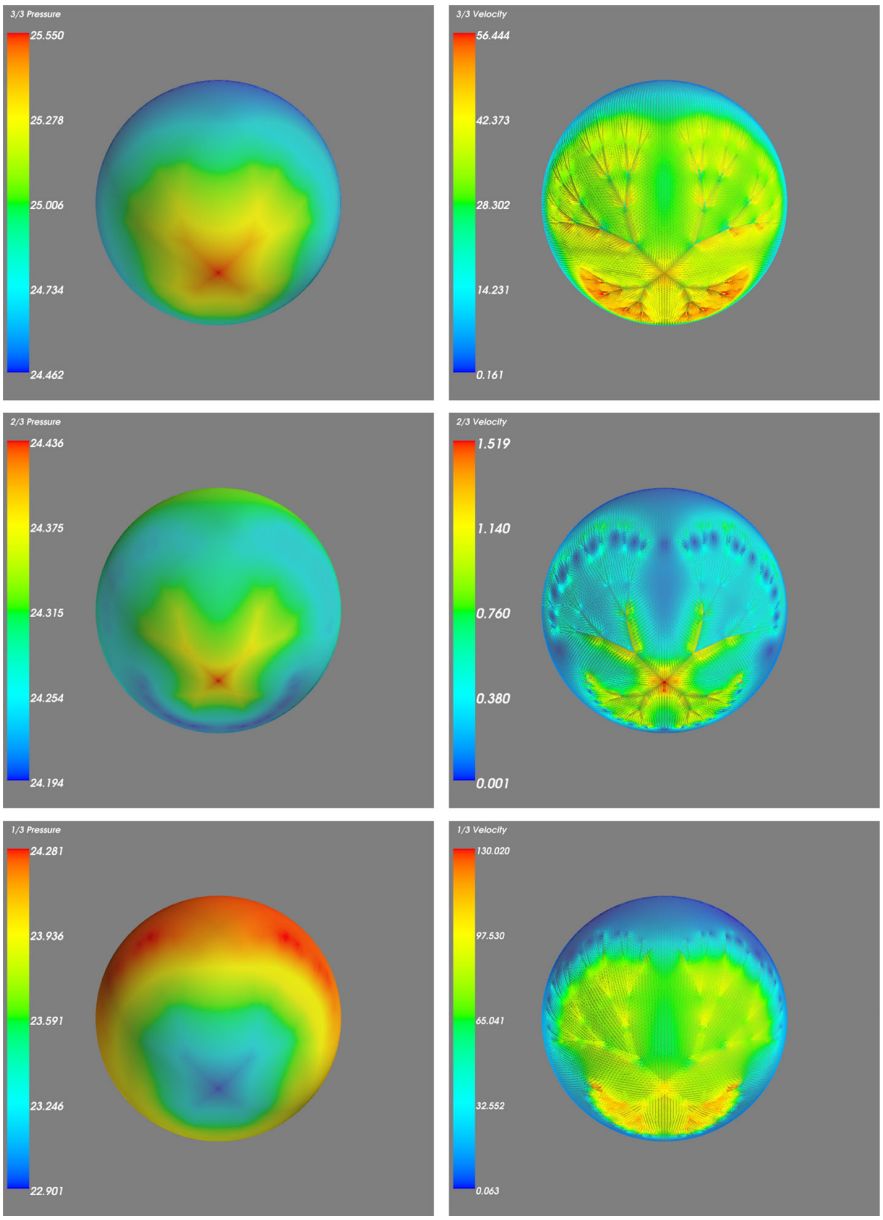

Fig. 10 Pressure fields in mmHg (*left*) and velocity fields in mm/s (*right*) for arterial, capillary and venous level. Binary tree with linear pressure distribution in each generation

for the automatic processing of fundus images is available in a variety of computational environments, including MATLAB (Mittal 2015), ImageJ (Abramoff et al. 2008) and ITK (Yoo et al. 2002).

An example of image-based vascular network reconstructed by our group using matched filters and local entropy thresholding, as in Chanwimaluang and Fan (2003), is reported in Fig. 11. Image extraction was performed on retinal images obtained from those archived in the DRIVE database and represents images from diabetic subjects (Staal et al. 2004). In order to integrate patient-specific vascular networks extracted from images into the retinal perfusion model two steps must still be completed. The algorithm is currently being extended to distinguish between arterioles and venules as required for simulations (Saeza et al. 2012). Once acquired, the extracted vascular geometry must then be mapped to the curved retinal surface.

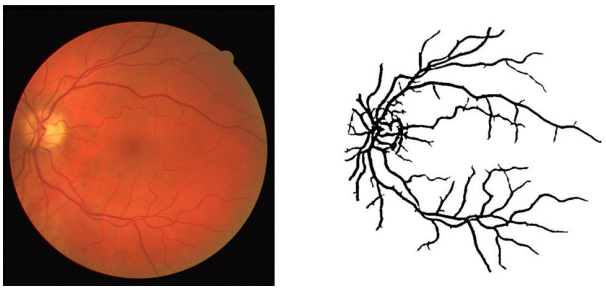

Fig. 11 Vascular extraction: original and extracted image

6 Conclusions and future perspectives

We have developed a computational framework to analyze the effect of ocular shape and vascular architecture on the retinal blood perfusion. The model predictions show that changes in ocular shape induce non-uniform alterations of pressure and velocity in the retina. In particular, we found that (i) the temporal region is affected the less by changes in ocular shape and that (ii) the barrel shape departs the most from the hemispherical reference geometry in terms of associated pressure and velocity distributions in the retinal microvasculature. These results support the clinical hypothesis that alterations in ocular shape, such as those occurring in myopic eyes, might be associated with pathological alterations in retinal hemodynamics. Physiologically reasonable results are also obtained in the case of more complex vascular geometries when the pressure is assumed to decrease linearly along the network. Thus, the computational framework developed in this paper might be useful for the design of more accurate theoretical and clinical studies taking into account image-based patient-specific ocular and vascular geometries.

The results presented in this paper encourage further investigation of the model from both the mathematical and computational viewpoints. Mathematically, the model parameter space comprises eight parameters when three hierarchical levels are considered, namely G_{a}, G_{v}, K_i and α_i, with $i = 0, 1, 2$. It would be very interesting to formally study the sensitivity of retinal hemodynamics on these parameters.

We remark that our numerical method computes blood pressure as primal variable. However, the measurement devices currently available permit measurement of blood velocity and not pressure. Computationally, the velocity can be obtained from the computed pressure in our current formulation. However, such a computation would result in loss of an order of accuracy (piecewise linear pressures will result in piecewise constant velocities). A better alternative, and one that we intend to pursue in future, is to solve a mixed formulation of the problem. This will allow us to formulate and solve for pressure and velocity simultaneously. All the computational and theoretical tools needed for such an approach exist for standard Poisson equation and will require some development to make those suitable for the hierarchical model that we are solving. In particular, it is not known how the stability of numerical methods for the spatial part of the discretization will interact with the stability of the θ variable discretization when mixed methods are used. Other possible future enhancements include the use of higher-order finite elements, time-dependent sources and the use of an anisotropic, spatially varying permeability tensor. The enhancements relating to permeability tensor may require new developments in the numerical methods we used. For example, the stiffness matrix will need to be computed taking into account the variability in the permeability tensor.

Acknowledgments We thank Alexandra Benavente-Perez and Muhammed Ali Alan for helpful discussions. We thank the students who participated in the SUNY STEM summer program 2014. This work has been partially supported by the NSF DMS-1224195, NSF CCF-1064429, NIH 1R21EY022101-01A1, a grant from Research to Prevent Blindness (RPB, NY, USA), an Indiana University Collaborative Research Grant of the Office of the Vice President for Research and the Chair Gutenberg funds.

References

Abramoff M, Niemeijer M, Suttorp-Schulten M, Viergever M, Russell S, Ginneken B (2008) Evaluation of a system for automatic detection of diabetic retinopathy from color fundus photographs in a large population of patients with diabetes. Diabetes Care 31(2):193–198

Arciero J, Harris A, Siesky BA, Amireskandari A, Gershuny V, Pickrell A, Guidoboni G (2013) Theoretical analysis of vascular regulatory mechanisms contributing to retinal blood flow autoregulation. Invest Ophthalmol Vis Sci 54(8):5584–5593

Arnold DN, Falk RS, Winther R (2010) Finite element exterior calculus: from hodge theory to numerical stability. Bull Am Math Soc 47(2):281354

Bell N, Hirani AN (2012) PyDEC: software and algorithms for discretization of exterior calculus. ACM Trans Math Softw 39(1):3

Benavente-Perez A, Hosking SL, Logan NS, Broadway DC (2010) Ocular blood flow measurements in healthy human myopic eyes. Graefes Arch Clin Exp Ophthalmol 248(11):1587–1594

Causin P, Guidoboni G, Harris A, Prada D, Sacco R, Terragni S (2014) A poroelastic model for the perfusion of the lamina cribrosa in the optic nerve head. Math Biosci 257:33–41

Chanwimaluang T, Fan G (2003) An efficient blood vessel detection algorithm for retinal images. In: IEEE international symposium on circuits and systems, Bangkok, Thailand, pp 21–24

Crosby-Nwaobi R, Heng LZ, Sivaprasad S (2012) Retinal vascular calibre, geometry and progression of diabetic retinopathy in type 2 diabetes mellitus. Ophthalmologica 228(2):84–92

Crosby-Nwaobi R, Heng LZ, Sivaprasad S, Cheung CY, Lamoureux E, Ikram MK, Sasongko MB, Ding J, Zheng Y, Mitchell P, Wang JJ, Wong TY (2012) Retinal vascular geometry in asian persons with diabetes and retinopathy. J Diabetes Sci Technol 6(3):595–605

D'Angelo C (2007) Multiscale modeling of metabolism and transport phenomena in living tissues. Dissertation. EPFL, Lausanne, Italy

Demlow A (2009) Higher-order finite element methods and pointwise error estimates for elliptic problems on surfaces. SIAM J Numer Anal 47(2):805–827. doi:10.1137/070708135

Demlow A, Dziuk G (2007) An adaptive finite element method for the Laplace–Beltrami operator on surfaces. SIAM J Numer Anal 45:421–442

Desbrun M, Hirani AN, Leok M, Marsden JE (2005) Discrete exterior calculus. pp 1–52. ArXiv preprint math/0508341

Dziuk G (1988) Finite Elements for the Beltrami operator on arbitrary surfaces. In: Hildebrandt S, Leis R (eds) Partial differential equations and calculus of variations. Lecture notes in mathematics, vol 1357. Springer, pp 142–155

Evans LC (1998) Partial differential equations (graduate studies in mathematics), vol. 19, American Mathematical Society

Fledelius HC, Goldschmidt E (2010) Optic disc appearance and retinal temporal vessel arcade geometry in high myopia, as based on follow-up data over 38 years. Acta Ophthalmol 88(5):514–520

Foster PJ, Jiang Y (2014) Epidemiology of myopia. Eye 28(2):202–208
Galassi F, Sodi A, Ucci F, Harris A, Chung HS (1998) Ocular haemodynamics in glaucoma associated with high myopia. Int Ophthalmol 22(5):299–305
Ganesan P, He S, Xu H (2010) Analysis of retinal circulation using an image-based network model of retinal vasculature. Microvasc Res 80(1):99–109
Ganesan P, He S, Xu H (2011) Development of an image-based model for capillary vasculature of retina. Comput Methods Progr Biomed 102(1):35–46
Geuzaine C, Remacle JF (2009) Gmsh: a three-dimensional finite element mesh generator with built-in pre- and post- processing facilities. Int J Numer Methods Eng 79(11):1309–1331
Gugleta K, Polunina A, Kochkorov A, Waldmann N, Portmann N, Katamay R, Flammer J, Orgul S (2013) Retinal neurovascular coupling in patients with glaucoma and ocular hypertension and its association with the level of glaucomatous damage. Graefes Arch Clin Exp Ophthalmol 251:1577–1585
Guidoboni G, Harris A, Cassani S, Arciero J, Siesky B, Amireskandari A, Tobe L, Egan P, Januleviciene I, Park J (2014) Intraocular pressure, blood pressure, and retinal blood flow autoregulation: a mathematical model to clarify their relationship and clinical relevance. Invest Ophthalmol Vis Sci 55(7):4105–4118
Habib MS, Al-Diri B, Hunter A, Steel DH (2014) The association between retinal vascular geometry changes and diabetic retinopathy and their role in prediction of progression–an exploratory study. BMC Ophthalmol 14:89
Hirani AN (2003) Discrete exterior calculus. PhD thesis, California Institute of Technology
Hirani AN, Nakshatrala KB, H CJ (2015) Numerical method for Darcy flow derived using Discrete Exterior Calculus. Int J Comput Methods Eng Sci Mech 16(3):151–169
Hsu CC, Chen SJ, Li AF, Lee FL (2014) Systolic blood pressure, choroidal thickness, and axial length in patients with myopic maculopathy. J Chin Med Assoc 77(9):487–491
Huyghe J, Arts T, Campen D, Reneman R (1992) Porous medium finite element model of the beating left ventricle. Am J Physiol 262(4):H1256–H1267
Koh V, Cheung CY, Zheng Y, Wong TY, Wong W, Aung T (2010) Relationship of retinal vascular tortuosity with the neuroretinal rim: the Singapore Malay eye study. Invest Ophthalmol Vis Sci 51(7):3736–3741
Leske MC (2007) Open-angle glaucoma—an epidemiologic overview. Ophthalmic Epidemiol 14(4):166–172
Lim LS, Cheung CY, Lin X, Mitchell P, Wong TY, Mei-Saw S (2011) Influence of refractive error and axial length on retinal vessel geometric characteristics. Invest Ophthalmol Vis Sci 52(2):669–678
Lin JY, Ho WL, Ger LP, Sheu SJ (2013) Analysis of factors correlated with the development of pseudophakic retinal detachment - a long-term study in a single medical center. Graefes Arch Clin Exp Ophthalmol 251(2):459–465
Liu D, Wood NB, Witt N, Hughes AD, Thom SA, Xu XY (2000) Computational analysis of oxygen transport in the retinal arterial network. Curr Eye Res 34(11):945–956
Mamikonian VR, Shmeleva-Demir OA, Kharlap SI, Andzhelova DV, Kazarian EE, Makashova NV, Galoian NS, Mazurova IV, Tatevosian AA, Karapetian AT (2013) Hemodynamic changes in myopia of different degrees. Vestn Oftalmol 129(6):24–27
Mittal D, Kumari K (2015) Automated detection and segmentation of drusen in retinal fundus images. Comput Electr Eng 47:82–95
Moriyama M, Ohno-Matsui K, Hayashi K, Shimada N, Yoshida T, Tokoro T, Morita I (2011) Topographic analyses of shape of eyes with pathologic myopia by high-resolution three-dimensional magnetic resonance imaging. Ophthalmology 118(8):1626–1637
Murray CD (1926) The physiological principle of minimum work I. The vascular system and the cost of blood volume. Proc Natl Acad Sci 12:207–214
Ramachandran P, Varoquaux G (2011) Mayavi: 3D visualization of scientific data. Comput Sci Eng 13(2):40–51
Sacco R, Causin P, Zunino P, Raimondi MT (2011) A multiphysics/multiscale numerical simulation of scaffold-based cartilage regeneration under interstitial perfusion in a bioreactor. Biomech Model Mechanobiol 10(4):577–589
Saeza M, González-Vázquezc S, González-Penedoc M, Antònia Barceló M, Pena-Seijod M, Coll de Tuerob G (2012) Development of an automated system to classify retinal vessels into arteries and veins. Comput Methods Progr Biomed 108:367376
Sherman TF (1981) On connecting large vessels to small: the meaning of Murray's law. J Gen Physiol 78:431–453
Shimada N, Ohno-Matsui K, Harino S, Yoshida T, Yasuzumi K, Kojima A, Kobayashi K, Futagami S, Tokoro T, Mochizuki M (2004) Reduction of retinal blood flow in high myopia. Graefes Arch Clin Exp Ophthalmol 242(4):284–288
Staal J, Abramoff M, Niemeijer M, Viergever M, van Ginneken B (2004) Ridge based vessel segmentation in color images of the retina. IEEE Trans Med Imaging 23:501–509
Takahashi T, Nagaoka T, Yanagida H, Saitoh T, Kamiya A, Hein T, Kuo L, Yoshida A (2009) A mathematical model for the distribution of hemodynamic parameters in the human retinal microvascular network. J Biorheol 23:77–86
Talu S (2013) Multifractal geometry in analysis and processing of digital retinal photographs for early diagnosis of human diabetic macular edema. Curr Eye Res 38(7):781–792
Tham YC, Cheng CY, Zheng Y, Aung T, Wong TY, Cheung CY (2013) Relationship between retinal vascular geometry with retinal nerve fiber layer and ganglion cell-inner plexiform layer in nonglaucomatous eyes. Invest Ophthalmol Vis Sci 54(12):7309–7316
Vankan WJ, Huyghe JM, Drost MR, Janssen JD, Huson A (1997) Finite element mixture model for hierachical porous media. Int J Numer Methods Eng 40:193–210
Wu R, Cheung CY, Saw SM, Mitchell P, Aung T, Wong TY (2013) Retinal vascular geometry and glaucoma: the singapore malay eye study. Ophthalmology 120:77–83
Yoo T, Ackerman M, Lorensen W, Schroeder W, Chalana V, Aylward S (2002) Engineering and algorithm design for an image processing API: a technical report on itk - the insight toolkit. In: Westwood J (ed) Proceedings of medicine meets virtual reality. IOS Press, Amsterdam, pp 586–592
Zafar SN, Qureshi N, Azad N, Khan A (2013) Retinal detachment in paediatric patients. J Coll Physicians Surg Pak 23(4):261–264